Optical image hiding based on chaotic vibration of deformable moiré grating

Guangqing Lu [a], Loreta Saunoriene [b], Sandra Aleksiene [b], Minvydas Ragulskis [a,b,*]

[a] School of Electrical and Information Engineering of Jinan University, 206 Qianshan Road, Zhuhai, 519070, Guangdong, PR China
[b] Research Group for Mathematical and Numerical Analysis of Dynamical Systems, Kaunas University of Technology, Studentu 50-146, Kaunas, LT-51368, Lithuania

ARTICLE INFO

Keywords:
Time-averaged moiré
Digital image hiding
Chaotic vibrations

ABSTRACT

Image hiding technique based on chaotic vibration of deformable moiré grating is presented in this paper. The embedded secret digital image is leaked in a form of a pattern of time-averaged moiré fringes when the deformable cover grating vibrates according to a chaotic law of motion with a predefined set of parameters. Computational experiments are used to demonstrate the features and the applicability of the proposed scheme.

1. Introduction

Theoretical and practical aspects of chaotic oscillations in optical systems are widely studied, reported in numerous publications and implemented in a variety of industrial applications. A good survey of many possible applications of chaos in optical science and engineering — including optical communication with chaotic lasers is presented in [1]. Spatial deterministic chaos in optical systems [2], optical phase-conjugation by high-frequency chaotic dynamics [3], chaotic computer generated holograms [4] — are just few of many examples of innovative applications of chaos in optics in general.

Another area where the interplay between optics and chaos yields many interesting applications is image encryption based on optical techniques. A good overview on optical image encryption is given in [5]. Many different optical image encryption techniques employing chaotic dynamics are discussed in [6–9].

As mentioned previously, chaotic processes are applied in different areas of optics. But the opposite is also true – optical techniques are used to visualize, interpret and assess chaotic phenomena. A seminal work in this area uses reflective spheres to produce chaotic light scattering and to demonstrate optical fractal geometry [10].

Optical techniques can be also used to assess and interpret oscillations, including chaotic oscillations. The importance of optical techniques capable to assess and monitor chaotic oscillations is predetermined by the fact that nonlinearity is an intrinsic feature of any real-world system. It is well known that the response of a nonlinear systems can be chaotic even if it is driven by harmonic excitation.

An optical technique comprising a cover stochastic moiré grating which leaks the secret image when the cover image is oscillated according to a predefined law of motion is presented in [11]. Conditionally, this image hiding scheme can be interpreted as dynamic visual cryptography (DVC) [12]. Chaotically oscillating non-deformable cover images (stochastic moiré gratings) can be used to assess the parameters of chaotic oscillations [13], to monitor the condition of systems performing chaotic vibrations [14]. However, non-deformable moiré gratings limit the applicability of such optical techniques. For example, the experimental implementation of the image hiding technique based on DVC and computer generated holography (CGH) [12] for optical monitoring of micro-electromechanical systems (MEMS) would require physical formation of diffractive optical elements (DOE) on the surface of oscillating components. Therefore, the main objective of this paper is to develop an image hiding scheme in deformable stochastic moiré gratings applicable for chaotic oscillations and to validate it in virtual optical environment.

The paper is structured as follows. Optical background and formal description of the formation of time-averaged moiré fringes is described in Section 2. Optical effects produced by chaotically vibrating deformable moiré gratings are investigated in Section 3. Image hiding scheme based on chaotically oscillating deformable moiré gratings is presented in Section 4. Concluding remarks are given in the final section.

* Corresponding author at: Research Group for Mathematical and Numerical Analysis of Dynamical Systems, Kaunas University of Technology, Studentu 50-146, Kaunas, LT-51368, Lithuania
E-mail address: minvydas.ragulskis@ktu.lt (M. Ragulskis).

2. Optical background

2.1. Harmonic oscillations, non-deformable moiré grating

One-dimensional harmonic moiré grating can be defined as a periodic variation of grayscale color [15,16]:

$$F(x) = \frac{1}{2} + \frac{1}{2}\cos\left(\frac{2\pi}{\lambda}x\right), \tag{1}$$

where x is the longitudinal coordinate and λ is the pitch of the moiré grating. The numerical value 0 of function $F(x)$ corresponds to black color, 1 — to white color, all intermediate values within the interval $(0; 1)$ correspond to appropriate grayscale levels.

Let us suppose that the moiré grating (Eq. (1)) is formed on the surface of a one-dimensional non-deformable body and is harmonically oscillated around the state of equilibrium according to the harmonic deflection function $A\sin(\omega t + \varphi)$ (A is the amplitude of harmonic oscillations, ω is the cyclic frequency, φ is the phase and t is time). Since every point of the non-deformable body oscillates with the same amplitude, one-dimensional time-averaged image reads [17]:

$$\begin{aligned} F_t(x) &= \lim_{T\to\infty}\frac{1}{T}\int_0^T \left(\frac{1}{2} + \frac{1}{2}\cos\left(\frac{2\pi}{\lambda}(x - A\sin(\omega t + \varphi))\right)\right) dt \\ &= \frac{1}{2} + \frac{1}{2}\cos\left(\frac{2\pi}{\lambda}x\right) J_0\left(\frac{2\pi}{\lambda}A\right), \end{aligned} \tag{2}$$

where T is the exposure time used for the time-averaging, J_0 is the zero order Bessel function of the first kind. It can be noted that oscillation frequency ω and phase φ have no influence on the formation of time-averaged image [15]. Time-averaged image becomes continuously gray when the amplitude of harmonic oscillations is set to:

$$A = \frac{\lambda}{2\pi} r_i, \tag{3}$$

where r_i is the ith root of the zero order Bessel function of the first kind. Fig. 1(a) illustrates the dynamics of one-dimensional non-deformable moiré grating during one period of harmonic oscillations at $A = \frac{\lambda}{2\pi} r_2$; Fig. 1(b) shows the time-averaged image of Fig. 1(a). One-dimensional time-averaged moiré images at increasing amplitude of oscillation are shown in Fig. 1(c) (note that time-averaged fringes do form at amplitudes corresponding to Eq. (3)). The standard deviation of time-averaged image around 0.5 reads [18]:

$$S\left(F_t(x)\right) = \frac{\sqrt{2}}{4}\left|J_0\left(\frac{2\pi}{\lambda}A\right)\right|. \tag{4}$$

Fig. 1(d) shows the variation of standard deviation of time-averaged moiré at increasing amplitudes of harmonic oscillations.

2.2. Harmonic oscillations, deformable moiré grating

Let us consider a harmonic moiré grating on the surface of one-dimensional deformable body. Let us assume that the deflection of the point x from the state of equilibrium is $u(x,t)$. Then the deformed moiré grating reads [19]:

$$F(x,t) = \frac{1}{2} + \frac{1}{2}\cos\left(\frac{2\pi}{\lambda}\mu(x,t)\right), \tag{5}$$

if only the independent variable x can be expressed from the relationship

$$x + u(x,t) = z \tag{6}$$

into the explicit form

$$x = \mu(z,t). \tag{7}$$

Let us assume that the space and time variables can be separated in the deflection function $u(x,t)$:

$$u(x,t) = a(x)\cdot g(t), \tag{8}$$

where $a(x)$ is the shape function of in-plane oscillations; $g(t)$ is the time process. Now let us linearize function $a(x)$ around the point $x = x_0$:

$$a(x) = a_0 + \dot{a}_0\left(x - x_0\right) + O\left(x - x_0\right)^2, \tag{9}$$

where $a_0 = a\left(x_0\right)$ and $\dot{a}_0 = \left.\frac{da(x)}{dx}\right|_{x=x_0}$. Eqs. (6), (8), (9) yield the relationship:

$$x \approx \frac{z - (a_0 - \dot{a}_0 x_0)g(t)}{1 + \dot{a}_0 g(t)}. \tag{10}$$

Thus the deformed moiré grating reads:

$$F(x,t) \approx \frac{1}{2} + \frac{1}{2}\cos\left(\frac{2\pi}{\lambda}\cdot\frac{x - \left(a_0 - \dot{a}_0 x_0\right)g(t)}{1 + \dot{a}_0 g(t)}\right). \tag{11}$$

Averaging of Eq. (11) in time yields:

$$F_t(x) \approx \frac{1}{2} + \frac{1}{2}\lim_{T\to\infty}\frac{1}{T}\int_0^T \cos\left(\frac{2\pi}{\lambda}\cdot\frac{x - \left(a_0 - \dot{a}_0 x_0\right)g(t)}{1 + \dot{a}_0 g(t)}\right) dt. \tag{12}$$

Note that if $a(x) = A = const$ and $g(t) = \sin(\omega t + \varphi)$, Eq. (12) results into Eq. (2). If the deformation field is linear $a(x) = Ax$ [19]:

$$F(x,t) = \frac{1}{2} + \frac{1}{2}\cos\left(\frac{2\pi}{\lambda}\cdot\frac{x}{1 + A\sin t}\right) \tag{13}$$

and time-averaging yields:

$$F_t(x) \approx \frac{1}{2} + \frac{1}{2}\cos\left(\frac{2\pi}{\lambda}x\right) J_0\left(\frac{2\pi}{\lambda}Ax\right). \tag{14}$$

Thus, time-averaged moiré fringes do form at $\frac{2\pi}{\lambda}Ax = r_i$, $i = 1, 2, \ldots$ (note the difference from Eq. (3)). Fig. 2 illustrates the formation of time-averaged moiré fringes for the deformable moiré grating. The left side of the grating is fixed motionlessly; the right side oscillates harmonically (amplitude A varies from 0 to 0.3 in the observation window). The pitch of the moiré grating at the state of equilibrium is $\lambda = 0.2$. Fig. 2(a) illustrates the motion of one-dimensional deformable moiré grating during one period of oscillations. Time-averaged image of Fig. 2(a) is presented in Fig. 2(b). Fig. 2(c) shows the time-averaged one-dimensional moiré gratings at increasing amplitudes A (the higher is the amplitude of harmonic oscillations, the larger number of moiré fringes is visible in the time-averaged image).

2.3. Chaotic oscillations, non-deformable moiré grating

Let us consider chaotic oscillations of a non-deformable moiré grating:

$$F_t(x) = \frac{1}{2} + \frac{1}{2}\lim_{T\to\infty}\frac{1}{T}\int_0^T \cos\left(\frac{2\pi}{\lambda}\left(x - \theta(t)\right)\right) dt, \tag{15}$$

where $\theta(t)$ is a time function determining chaotic deflection from the state of equilibrium. If $\theta(t)$ is a Gaussian normal ergodic process, approximated by a discrete scalar series of normally distributed numbers with zero mean and σ^2 variance, the time-averaged image reads [20]:

$$F_t(x) = \frac{1}{2} + \frac{1}{2}\cos\left(\frac{2\pi}{\lambda}x\right)\exp\left(-\frac{1}{2}\left(\frac{2\pi}{\lambda}A\sigma\right)^2\right), \tag{16}$$

and time-averaged fringes do not form at all [20].

Standard deviation of the grayscale intensity of time-averaged moiré (Eq. (16)) reads:

$$S(F_t(x)) = \frac{1}{\lambda}\int_0^{\lambda}\left(F_t(x) - E\left(F_t(x)\right)\right)^2 dx = \frac{\sqrt{2}}{4}\exp\left(-\frac{1}{2}\left(\frac{2\pi}{\lambda}A\sigma\right)^2\right), \tag{17}$$

However, it is difficult to construct a clear physical interpretation for the replacement of a continuous chaotic function by a discrete scalar series of normally distributed numbers (though such a replacement is beneficial for building theoretical relationships). Therefore we continue

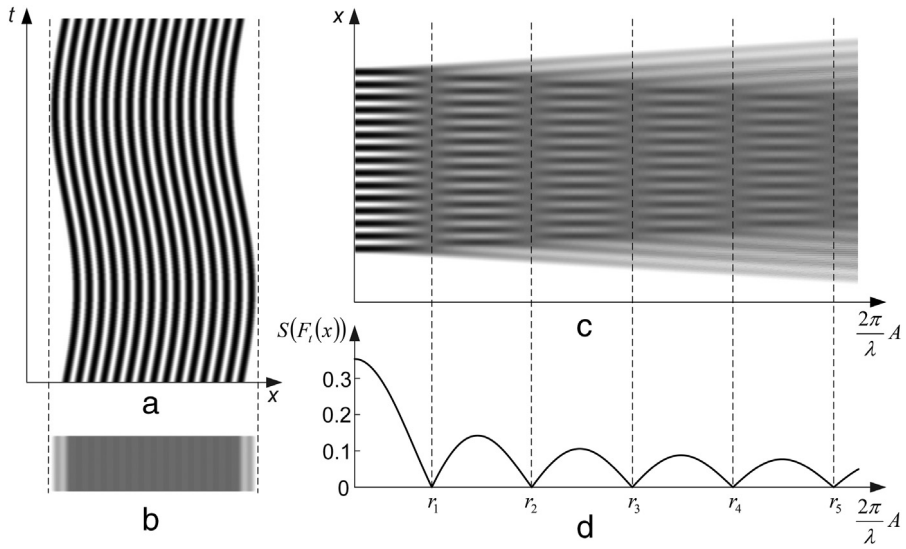

Fig. 1. Time-averaged moiré fringes produced by harmonic oscillations of one-dimensional non-deformable moiré grating ($\lambda = 0.2$): (a) motion of one-dimensional moiré grating during one period of oscillations ($A = \frac{\lambda}{2\pi} r_2$); dashed lines indicate maximum displacements from the state of equilibrium; (b) time-averaged image of part (a); (c) time-averaged one-dimensional images of the moiré grating at increasing amplitudes A; (d) standard deviation of time-averaged images; dashed lines illustrate the centers of time-averaged fringes and the zeros of standard deviation function.

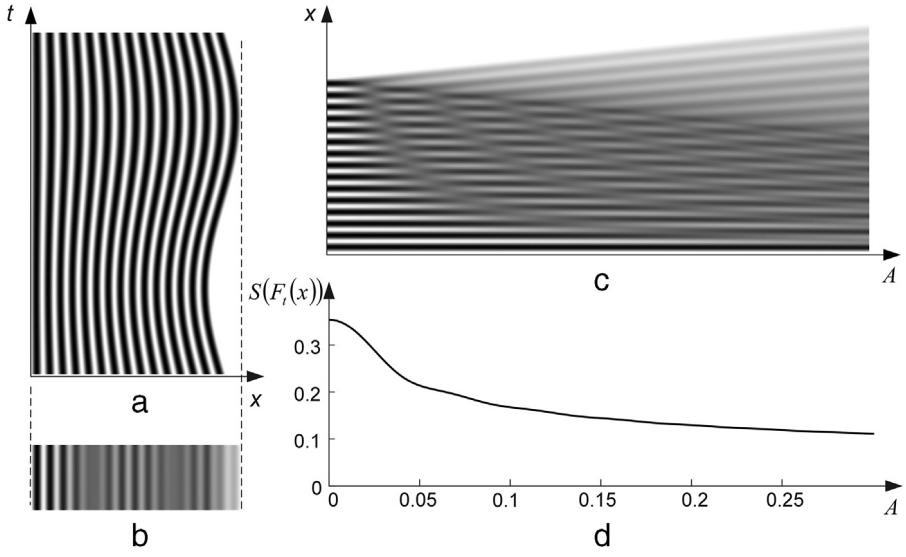

Fig. 2. Time-averaged image of the deformable one-dimensional moiré grating. The pitch of the grating in the state of equilibrium is $\lambda = 0.2$. (a) motion of one-dimensional moiré grating during one period of oscillations ($A = 0.075$; dashed line indicate maximum displacement from the state of equilibrium); (b) time-averaged image of part (a); (c) one-dimensional time-averaged moiré grating at increasing amplitudes A; (d) standard deviation of the time-averaged image.

by assuming that $\theta(t)$ is a solution of the paradigmatic chaotic model — the Rossler system [21]:

$$\begin{aligned} \frac{dx_1}{dt} &= -x_2 - x_3 \\ \frac{dx_2}{dt} &= x_1 + ax_2, \\ \frac{dx_3}{dt} &= bx_1 - cx_3 + x_1 x_3, \end{aligned} \tag{18}$$

where x_1, x_2, x_3 are functions of time t; a, b, c are constant parameters. The Rossler system exhibits stationary, periodic, quasiperiodic, and chaotic behavior at different values of the parameters. Chaotic attractor of the Rossler system at $a = 0.3$, $b = 0.2$, $c = 5.7$ is shown in Fig. 3.

Let us suppose that the analyzed one-dimensional non-deformable body oscillates around the state of equilibrium according to the time function $Ax_1(t)$ (Eq. (18)) where A is a constant. Fig. 4(a) illustrates chaotic oscillation of one-dimensional moiré grating at $A = 0.09$. Time-averaging of Fig. 4(a) yields Fig. 4(b). One-dimensional time-averaged images at increasing values of A are shown in Fig. 4(c).

3. Optical effects produced by a chaotically oscillating deformable moiré grating

As mentioned previously, the main objective of this paper is to develop an image hiding scheme in chaotically oscillating deformable moiré gratings. The derivation of theoretical relationships determining the formation of time-averaged moiré fringes (when the deformable grating performs chaotic oscillations) is required before the image hiding scheme could be constructed.

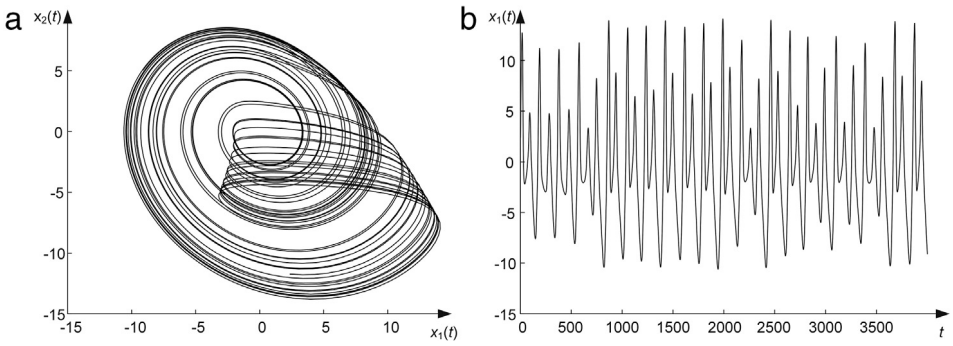

Fig. 3. The solution of the Rossler system in a steady state at $a = 0.3$, $b = 0.2$ and $c = 5.7$; (a) chaotic attractor in the phase plane $x_1 - x_2$; (b) $x_1(t)$.

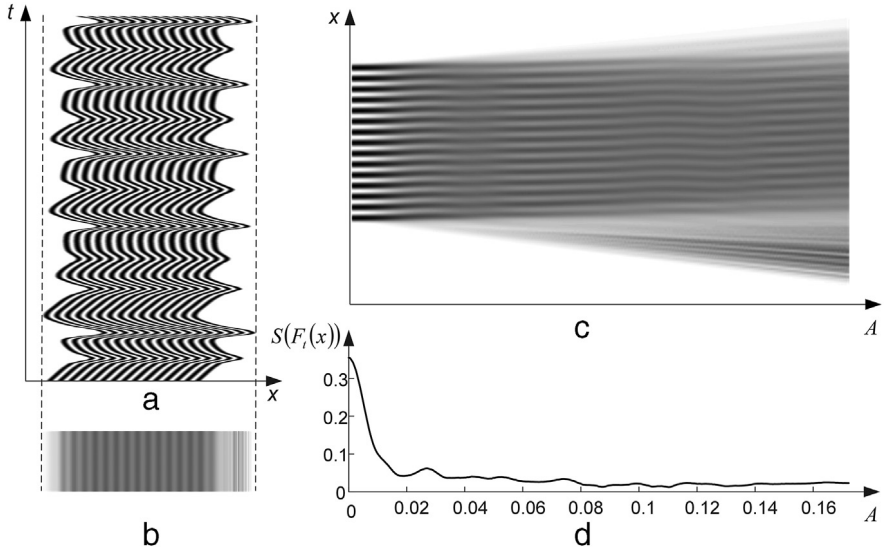

Fig. 4. Chaotic oscillations of non-deformable one-dimensional moiré grating at $\lambda = 0.2$: (a) chaotic oscillation according to the time function $Ax_1(t)$ ($A = 0.09$); dashed lines determine maximum deflections from the state of equilibrium; (b) time-averaged image of part (a); (c) one-dimensional time-averaged images at increasing values of A; (d) standard deviation of the time-averaged image.

3.1. Linear shape function a(x)

Let us consider a deformable one-dimensional moiré grating with a constant pitch in the state of equilibrium $\lambda = 0.2$. Let us assume that the left side of the moiré grating is fixed, the right side is oscillating according to the chaotic time function $g(t) = Ax_1(t)$. Moreover, let the shape function of in-plane oscillations be linear: $a(x) = x$. Then,

$$F(x,t) = \frac{1}{2} + \frac{1}{2}\cos\left(\frac{2\pi}{\lambda}\cdot\frac{x}{1+Ax_1(t)}\right), \tag{19}$$

where the parameter A varies from 0 to 0.02 (Fig. 5). The resulting time-averaged images are illustrated in Fig. 5(c). Note that the standard deviation of the time-averaged images in Fig. 5(c) is higher than in Fig. 4(c). This can be explained by the fact that the left side of the deformable grating is motionlessly fixed.

3.2. Nonlinear shape function a(x)

Let us analyze the case when the shape function describing the oscillation mode of a deformable one-dimensional body is nonlinear. The argument of cosine function in Eq. (12) can be rearranged as follows:

$$\begin{aligned}\frac{x-\left(a_0-\dot{a}_0x_0\right)g(t)}{1+\dot{a}_0g(t)} &= \left(x-\left(a_0-\dot{a}_0x_0\right)g(t)\right)\cdot\frac{1}{1+\dot{a}_0g(t)}\\ &= \left(x-(a_0-\dot{a}_0x_0)g(t)\right)\left(1-\dot{a}_0g(t)\right)+O(\dot{a}_0^2).\end{aligned} \tag{20}$$

Let us denote $a_0+\dot{a}_0\left(x-x_0\right) = \bar{a}(x)$. Then the deformed moiré grating reads:

$$\begin{aligned}F(x,t) \approx{}& \frac{1}{2}+\frac{1}{2}\cos\left(\frac{2\pi}{\lambda}\cdot\left(x-\left(a_0-\dot{a}_0x_0\right)g(t)-\dot{a}_0xg(t)\right.\right.\\ &\left.\left.+\left(a_0-\dot{a}_0x_0\right)\dot{a}_0g^2(t)\right)\right)\\ ={}& \frac{1}{2}+\frac{1}{2}\cos\left(\frac{2\pi}{\lambda}\cdot\left(\left(x+(a_0-\dot{a}_0x_0)\dot{a}_0g^2(t)\right)\right.\right.\\ &\left.\left.-(a_0+\dot{a}_0(x-x_0))g(t)\right)\right)\\ ={}& \frac{1}{2}+\frac{1}{2}\cos\left(\frac{2\pi}{\lambda}\cdot\left(x+\left(a_0-\dot{a}_0x_0\right)\dot{a}_0g^2(t)\right)\right)\\ &\times\cos\left(\frac{2\pi}{\lambda}\cdot\bar{a}(x)g(t)\right)\\ &+\frac{1}{2}\sin\left(\frac{2\pi}{\lambda}\cdot\left(x+\left(a_0-\dot{a}_0x_0\right)\dot{a}_0g^2(t)\right)\right)\\ &\times\sin\left(\frac{2\pi}{\lambda}\cdot\bar{a}(x)g(t)\right).\end{aligned} \tag{21}$$

Time-averaging of Eq. (21) yields:

$$\begin{aligned}F_t(x) &= \lim_{T\to\infty}\frac{1}{T}\int_0^T F(x,t)\,dt =\\ &= \frac{1}{2}+\frac{1}{2}\lim_{T\to\infty}\frac{1}{T}\int_0^T\cos\left(\frac{2\pi}{\lambda}\cdot\left(x+(a_0-\dot{a}_0x_0)\dot{a}_0g^2(t)\right)\right)\\ &\times\cos\left(\frac{2\pi}{\lambda}\cdot\bar{a}(x)g(t)\right)dt\end{aligned}$$

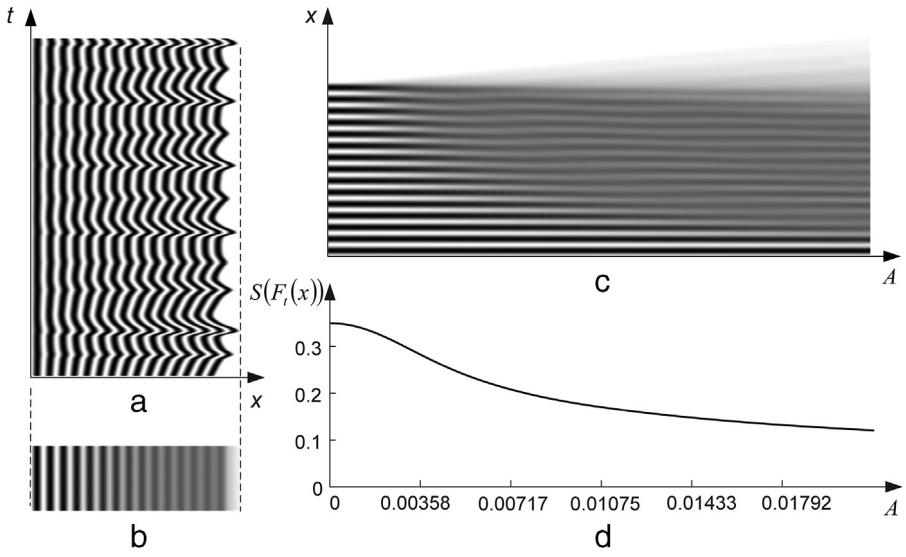

Fig. 5. Time-averaged image of the deformable one-dimensional moiré grating at $a(x) = x$ and $g(t) = Ax_1(t)$: (a) chaotic motion of one-dimensional moiré grating at $A = 0.005$; (b) time-averaged image of part (a); (c) one-dimensional time-averaged moiré grating at different values of A; (d) standard deviation of time-averaged one-dimensional images.

$$+\frac{1}{2}\lim_{T\to\infty}\frac{1}{T}\int_0^T \sin\left(\frac{2\pi}{\lambda}\cdot\left(x+(a_0-\dot{a}_0x_0)\dot{a}_0g^2(t)\right)\right)$$
$$\times\sin\left(\frac{2\pi}{\lambda}\cdot\bar{a}(x)\,g(t)\right)dt. \tag{22}$$

If the time function $g(t)$ is the Gaussian normal ergodic process, it can be approximated by a discrete scalar series of normally distributed numbers with zero mean and σ^2 variance:

$$g_i \sim N(0,\sigma), \quad i = 1,2,\ldots,k. \tag{23}$$

Then in correspondence to [20] the following approximations hold true:

$$\lim_{T\to\infty}\frac{1}{T}\int_0^T \cos\left(\frac{2\pi}{\lambda}\cdot\bar{a}(x)\,g(t)\right)dt = \exp\left(-\frac{1}{2}\left(\frac{2\pi}{\lambda}\cdot\bar{a}(x)\,\sigma\right)^2\right)$$
$$\lim_{T\to\infty}\frac{1}{T}\int_0^T \sin\left(\frac{2\pi}{\lambda}\cdot\bar{a}(x)\,g(t)\right)dt = 0. \tag{24}$$

But, if g_i are normally distributed numbers with zero mean and σ^2 variance, then g_i^2 are distributed according to chi-squared distribution ($g_i^2 \sim \chi^2(1)$) and $Eg_i^2 = \sigma^2$ [22]. Now, Eq. (22) can be rearranged by replacing $g^2(t)$ by σ^2 and keeping approximations in Eq. (24) in force:

$$F_t(x) \approx \frac{1}{2}+\frac{1}{2}\cos\left(\frac{2\pi}{\lambda}\left(x+\left(a_0-\dot{a}_0x_0\right)\dot{a}_0\sigma^2\right)\right)$$
$$\times\exp\left(-\frac{1}{2}\left(\frac{2\pi}{\lambda}\cdot\bar{a}(x)\,\sigma\right)^2\right). \tag{25}$$

The obtained relationship in Eq. (25) corresponds well with the Eq. (16). It is clear that in case of stochastic oscillations time-averaged fringes do not form at all. Higher variance and/or higher values of maximum deflections yield more intensive blur. However, this relationship is only approximate since it was derived under the assumptions that $g^2(t)$ can be replaced by σ^2.

3.3. Computational validation of Eq. (25)

Computational experiments are used to validate the obtained approximate relationship in Eq. (25). Let us consider a deformable one-dimensional moiré grating with both the left and the right sides motionlessly fixed in the observation window $0 \le x \le L$. The shape function $a(x)$ is assumed to represent the first mode of the deformable one-dimensional body:

$$a(x) = \sin\left(\frac{\pi x}{L}\right). \tag{26}$$

It is clear that a deformable moiré grating with a constant pitch cannot result into a uniform time-averaged image throughout the observation window simply because different points of the grating oscillate with different amplitudes (Figs. 2 and 5). Therefore, a proper selection of the pitch of the moiré grating (in the state of equilibrium) is the first step for the validation of Eq. (25). The variable pitch of the grating must be proportional to the shape function [19]. Therefore, we assume that

$$\lambda(x) = 3\sin\left(\frac{\pi x}{L}\right). \tag{27}$$

The deformable moiré grating in the state of equilibrium is shown in Fig. 6 (parts (a), (b) and (c)) at $A = 0$. Fig. 6(a) illustrates time-averaged images of the one-dimensional deformable moiré grating when the time function $g(t)$ is approximated as a Gaussian normal ergodic process (Eq. (23)) with standard deviation σ equal to 0.7; the number of discrete values of $g(t)$ used for time-averaging is preselected to $k = 5000$.

Analogously, Fig. 6(b) shows time-averaged images when the time function $g(t) = Ax_1(t)$; the number of discrete values of $g(t)$ used for time-averaging is preselected to $k = 20\,000$. Finally, Fig. 6(c) illustrates time-averaged images as defined by Eq. (25) (σ is set to 0.7).

The variation of the standard deviation of the time-averaged image in Fig. 6(a) is shown in Fig. 7 (the densely dashed line at $k = 5000$). However, in order to demonstrate optical effects of time-averaging, we visualize standard deviations also at $k = 100$ and $k = 1000$ (Fig. 7). Analogously, standard deviations of Fig. 6(b) and (c) are also illustrated in Fig. 7. It is clear that the Gaussian approximation of the chaotic process converges to the theoretical approximation (Eq. (25)) when k is increased. Moreover, the representation of the chaotic process by Rossler time series also yields a rather good correspondence to Eq. (25). The differences at higher values of the parameter A can be explained by the limited exposure time used to generate the time-averaged image.

4. Dynamic visual cryptography based on chaotically oscillating deformable moiré gratings

4.1. Image hiding in chaotically oscillating deformable one-dimensional moiré grating

Image hiding techniques in stochastic non-deformable moiré gratings are based on the dichotomous representation of the secret image [11]. One pitch of the moiré grating is used for the representation of the background — a slightly different pitch of another moiré grating is used for the representation of the secret. Chaotic phase scrambling is

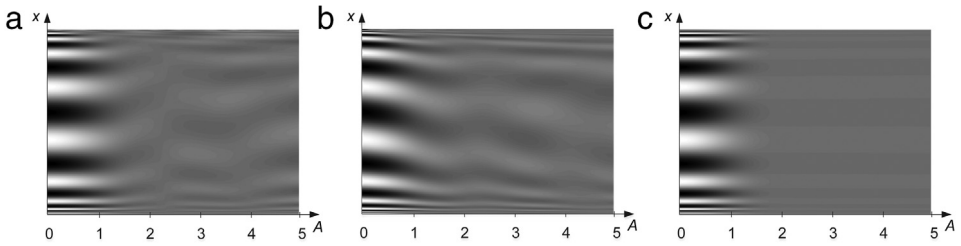

Fig. 6. Time-averaged images of one-dimensional deformable moiré grating oscillating according to the first Eigenmode: (a) $g(t)$ is approximated by $g_i \sim A \cdot N(0, 0.7)$; (b) $g(t) = Ax_1(t)$ where $x_1(t)$ is the chaotic Rossler process; (c) analytical result produced by Eq. (25) at $\sigma = 0.7$.

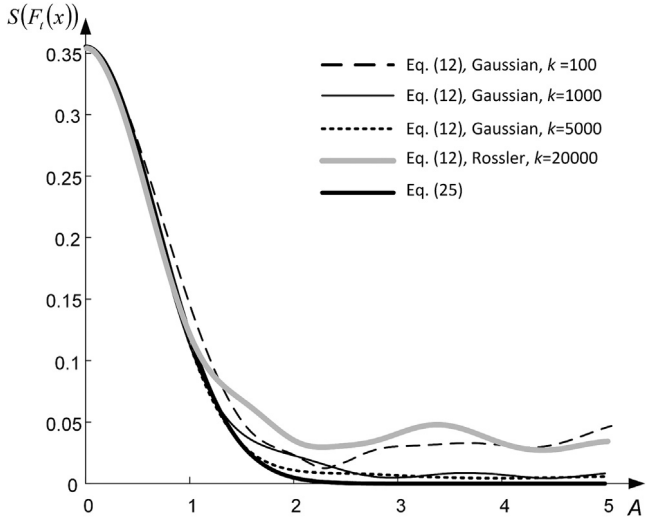

Fig. 7. Standard deviations of time-averaged one-dimensional moiré images.

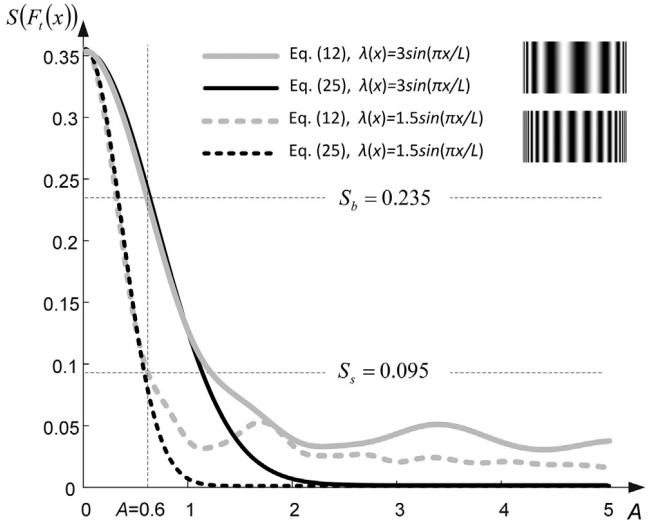

Fig. 8. Standard deviations of time-averaged one-dimensional moiré images with different pitches.

used to conceal the secret in the cover image. The secret is leaked in the form of a pattern of time-averaged moiré fringes when the cover image is oscillated according to a predefined law of motion.

However, as demonstrated in previous examples, time-averaged moiré fringes do not form when the deformable moiré grating is oscillated according to a chaotic law of motion. Anyway, we will use the dichotomous secret image representation by using different pitches for the secret and the background. Let us continue with the computational example used for the validation of Eq. (25). Let the variable pitch for one deformable moiré grating be $\lambda(x) = 3\sin\left(\frac{\pi x}{L}\right)$ and the pitch for the other moiré grating — $\lambda(x) = 1.5\sin\left(\frac{\pi x}{L}\right)$. The standards of time-averaged moiré gratings oscillating according to a chaotic law of motion are shown in Fig. 8.

Now, it is possible to select such a value of parameter A that the difference between the standards of both gratings would be large enough ($A = 0.6$ in Fig. 8). The secret will be leaked in the time-averaged image when the cover image is oscillated according to the time function describing the chaotic Rossler attractor. The roughness of the blurred time-averaged image will be different in the areas occupied by the background and by the secret image. This difference should be large enough to ensure sufficient contrast between the secret and the background in the time-averaged image.

If the variable pitch of the moiré grating in the area occupied by the secret image is $\lambda_s(x) = 1.5\sin\left(\frac{\pi x}{L}\right)$, then standard deviation is equal to $S_s = 0.095$ at $A = 0.6$ (the areas of the time-averaged cover image occupied by the secret are almost completely blurred). But if the pitch of the grating in the background is $\lambda_b(x) = 3\sin\left(\frac{\pi x}{L}\right)$, then the time-averaged image of the background is still very rough ($S_b = 0.235$). The difference between standard deviations in the background and in the secret area in this case is $|S_s - S_b| = 0.14$, what ensures the sufficient contrast between the secret and the background in time-averaged image (Fig. 8). But if the parameter A would be higher than 1.5, the difference between standard deviations $|S_s - S_b|$ would be too small for visual interpretation of the secret image (Fig. 8).

4.2. The description of the image hiding scheme

The physical implementation of the image hiding scheme comprises two steps. The first step is the phase regularization at the boundaries between the secret image and the background. The second step is the chaotic scrambling of initial phases. Both steps are illustrated in Fig. 9.

Let us consider a one-dimensional deformable moiré grating defined by a discontinuous shape function (Fig. 9(a)). The observation window ($0 \le x \le 10$) is split into three parts. Without losing the generality, let us assume that the secret image corresponds to the middle part (the other two parts stand for the background).

Previous derivations require that the variable pitch of the moiré grating must be proportional to the shape function. Therefore, a straightforward optical encoding of a discontinuous shape function would result into discontinuous variation of the phase of the moiré grating (Fig. 9(b)). Such discontinuities could compromise the hiding scheme as the boundaries between the secret image and the background could be recognizable by a naked eye. Thus, it is necessary to implement the regularization of phases at the boundaries. This step is illustrated in Fig. 9(c).

Note that the phase of the deformable moiré grating at the left part of the one-dimensional image is left unchanged (if compared to Fig. 9(b)). However, the initial phase of the grating in the middle part is adjusted in such a way that the composite moiré grating becomes continuous (Fig. 9(c)). Note that the adjustment of the initial phase does not alter

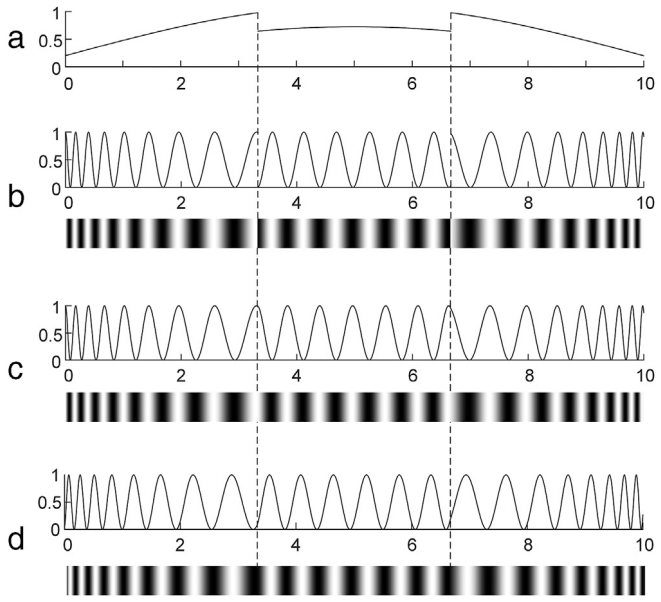

Fig. 9. A schematic diagram illustrating the proposed image hiding scheme. A typical shape function is shown in part (a); one-dimensional moiré grating without and with phase regularization — in parts (b) and (c); one-dimensional moiré grating with a randomly selected initial phase — in part (d).

the predetermined variable pitch of the grating. The same procedure of phase regularization is repeated at the other boundary (between the center and the right parts). Note that there are no limitations to the number of regularized boundaries, unless the order of the regularization is preserved.

The next step of the proposed image hiding technique is the chaotic scrambling of initial phases. Let us consider two adjacent columns of grayscale pixels. The pixels in those columns would be identical if the shape function is a slowly varying function. This optical effect (and the image hiding scheme in general) is illustrated in Fig. 10. For simplicity let us consider a secret image as a black square in the white background (Fig. 10(a)). Also, let us consider that the two-dimensional shape function is not constant in the window of observation. The straightforward embedding of the secret into the background results into a deformable moiré grating which can be interpreted by a naked eye (Fig. 10(b)). The regularization of phases at the horizontal boundaries between the secret and the background eliminates discontinuities at each individual column of pixels (Fig. 10(c)). Finally, chaotic scrambling of initial phases for each column of pixels results into an uninterpretable cover image (Fig. 10(d)).

4.3. The information capacity of the image hiding scheme

It has been demonstrated in the previous sections that the variable pitch $\lambda(x)$ must be proportional to the shape function $a(x)$. This proportionality is determined by the mathematical properties of the time-averaging operator and the physical properties of the chaotic oscillations. However, a particular selection of the variable pitch is directly related to the image hiding effect and the information capacity of the image hiding scheme.

Let us consider the same example as used to illustrate the image hiding scheme in Fig. 10. However, the size of the square element is different now (Fig. 11). The pitch of the moiré grating is variable in the observation window. Nevertheless, we use the mean value of the pitch and construct four computational experiments. Fig. 11(a) represents a square element embedded in the center of the cover image; the length of the side of this element is equal to $0.25\bar{\lambda}$ ($\bar{\lambda}$ is the mean pitch in the observation window). The top image is the time-averaged cover image performing chaotic oscillations according to the predefined shape function. The bottom image is the contrast enhanced time-averaged cover image.

Analogously, computational experiments with a square element with the side length equal to $0.5\bar{\lambda}$ is illustrated in Fig. 11(b); $\bar{\lambda}$ — in Fig. 11(c), and $2\bar{\lambda}$ — in Fig. 11(d). Thus, the minimum size of an element to be interpretable in the time-averaged image must be not smaller than a half of the mean pitch (Fig. 11).

This limitation predetermines the information capacity of the image hiding scheme. Note that the variable pitch $\lambda(x)$ of the cover image must be carefully preselected according to the physical parameters of the chaotic oscillator (the shape function predetermines the field of amplitudes; the variance predetermines the randomness of the chaotic process). Once the variable pitch $\lambda(x)$ is fixed, it is possible to assess the information capacity of the cover image — and to design the secret image itself.

4.4. The security of the image hiding scheme

As mentioned previously, the proposed image hiding scheme belongs to the class of visual cryptography techniques – special algorithms are required to encode the image, but decoding does not require a computational device and is completely visual. Classical visual cryptography schemes are based on the splitting of the secret image into several shares. Each share separately is cryptographically secure — the secret is leaked when all shares are accurately overlaid on top of each other. However, the secret image is not split into shares in the proposed scheme. Only one cover image is used, and the secret is leaked in the time-averaged image.

It is natural that every image hiding scheme has some advantages and drawbacks. As mentioned previously, classical visual cryptography schemes are cryptographically secure — but special algorithms must be used for minimizing the probability of cheating [23].

The proposed image hiding scheme is not strictly cryptographically secure — the secret image is directly leaked from the single cover image in the time-averaged mode. Moreover, shape functions with different coefficients of proportionality are used for the background and for the areas occupied by the secret. Let us consider a simplified situation when shape functions are constant in the whole window of observation. Such a situation would result into deformable moiré gratings with constant pitches in the state of equilibrium. Let the pitch in the area occupied by the secret image be λ_s, and the pitch in the background — λ_b.

It is clear that pitches λ_s and λ_b cannot differ very significantly — otherwise the encoded secret could be observed by a naked eye in

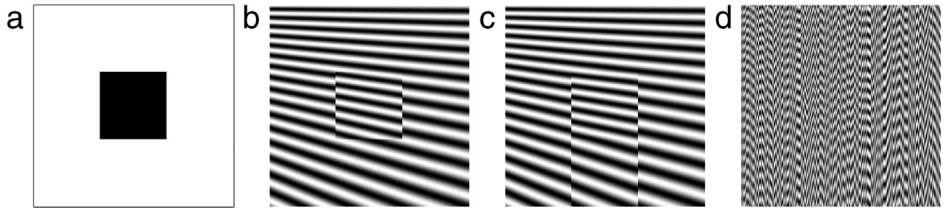

Fig. 10. A schematic diagram illustrating the proposed image hiding scheme; the pitch $\lambda(x)$ varies in the interval $[0.2; 0.4]$ in the observation window. A straightforward embedding of the secret image (part (a)) into the background is shown in part (b). Phase regularization is demonstrated in part (c); stochastic scrambling of initial phases – in part (d).

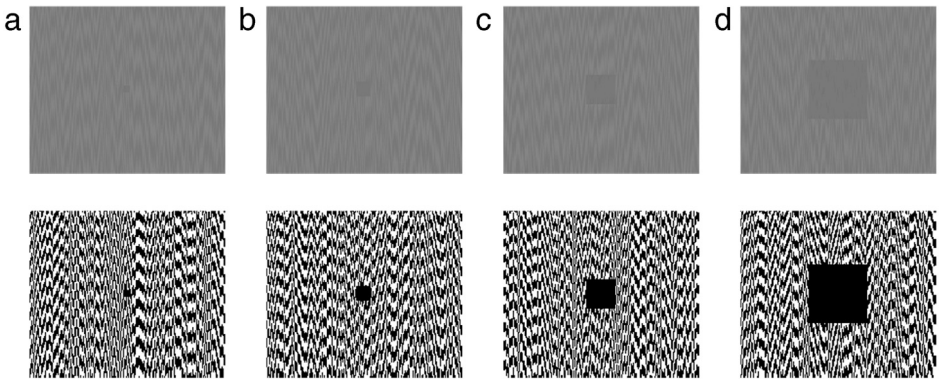

Fig. 11. The information capacity of the image hiding scheme. Figures in the top row represent time-averaged images of a deformable moiré grating performing chaotic oscillations according to the shape function used in Fig. 10; figures in the bottom row — appropriate contrast enhanced images. The size of the side of the square secret element is $0.25\bar{\lambda}$ (part (a)); $0.5\bar{\lambda}$ (part (b)); $\bar{\lambda}$ (part (c)) and $2\bar{\lambda}$ (part (d)), where $\bar{\lambda}$ is the mean pitch in the observation window.

the static cover image. On the other hand, the difference between λ_s and λ_b should ensure a sufficient contrast between the secret and the background in the time-averaged image. Note that vibrations of the deformable cover image are chaotic. Thus, the standard deviation of the grayscale color around 0.5 in the time-averaged image is $\sigma_s = \frac{\sqrt{2}}{4}\exp\left(-\frac{1}{2}\left(\frac{2\pi}{\lambda_s}A\sigma\right)^2\right)$ in the zone occupied by the secret, and $\sigma_b = \frac{\sqrt{2}}{4}\exp\left(-\frac{1}{2}\left(\frac{2\pi}{\lambda_b}A\sigma\right)^2\right)$ in the background (Eq. (17)).

The secret is leaked when a sufficient contrast between σ_s and σ_b is obtained in the time-averaged image. Let us assume that time-averaged moiré fringes become almost fully developed in the regions occupied by the secret ($\sigma_s = \varepsilon$, where ε is a small positive number). Then, the standard deviation of the background should be as large as possible: $|\sigma_b - \sigma_s| = |\sigma_b - \varepsilon| \geq \delta$. Note that $\lambda_s = \frac{\sqrt{2}\pi A\sigma}{\sqrt{-\ln\left(2\sqrt{2}\varepsilon\right)}}$ (because $\sigma_s = \varepsilon$). Therefore, the following inequality must hold true when $\sigma_b > \sigma_s$:

$$\lambda_b \geq \frac{\sqrt{2}\pi A\sigma}{\sqrt{-\ln\left(2\sqrt{2}(\varepsilon+\delta)\right)}}. \tag{28}$$

Analogously, when $\sigma_b < \sigma_s$:

$$\lambda_b \leq \frac{\sqrt{2}\pi A\sigma}{\sqrt{-\ln\left(2\sqrt{2}(\varepsilon-\delta)\right)}}. \tag{29}$$

Graphical interpretations of these inequalities are illustrated in Fig. 12. This is a standard optimization problem with constraints — find $\max\delta$ (maximum difference between contrasts in the time averaged image) at a minimum difference between λ_s and λ_b (minimum differences of pitches in the static cover image). The Pareto optimal frontier is illustrated in Fig. 12 by a thick solid line. Thus, if ε is set to 0.05, λ_s is 3.18 mm, the difference $|\sigma_b - \sigma_s|$ should be not smaller than 0.1, then λ_b must be not smaller than 4.8 mm (Fig. 12).

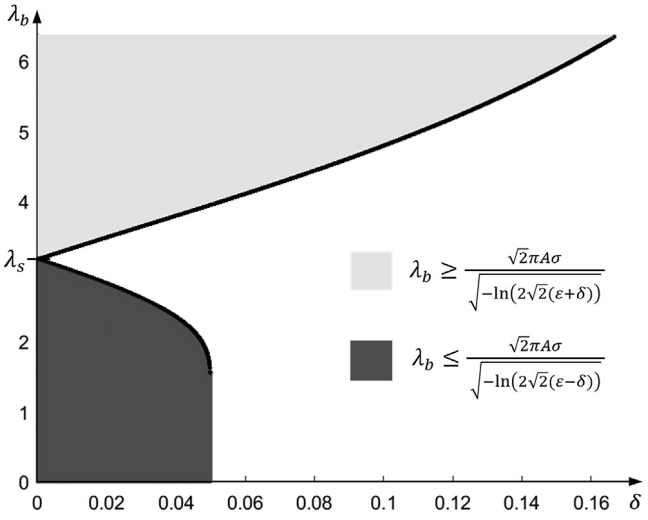

Fig. 12. Graphical interpretations of inequalities Eqs. (28) and (29) at $\varepsilon = 0.05$, $A = 1$, $\sigma = 1$ (thick solid line stands for the Pareto optimal frontier).

4.5. The construction of 2D moiré grating and the virtual optical setup

Let us consider a virtual optical setup where the moiré grating is formed on the reflective surface of a deformable plate. Without losing the generality we assume the paraxial illumination perpendicular to the surface of the plate in the state of equilibrium; the reflected moiré image is recorded directly above the surface of the plate. Let us consider the 17th two-dimensional shape function describing natural oscillations of a free deformable plate (Fig. 13(a)).

The 2D moiré grating on the surface of the plate in the plane equilibrium is formed as an array of parallel one-dimensional moiré gratings. If all one-dimensional moiré gratings would have the same and the constant pitch, and the initial phase of all one-dimensional gratings would be equal, the composite 2D moiré image would represent and array of parallel dark and bright constitutive bands perpendicular to the direction of 1D gratings.

However, as discussed in Section 3.3, the pitch of every 1D moiré grating must be variable (and must be proportional to the shape function defining the appropriate mode of oscillations). Let us consider the centerline of the 2D shape function (shown as a 1D function in Fig. 14(a)). Fig. 14(b) shows the absolute values of the shape function. But the linear relationship between the modulus of the shape function and the pitch implies that the pitch of 1D moiré grating must be zero at the nodal points of the Eigenshape. Clearly, the physical construction of a moiré grating with an infinitesimal pitch is not possible. Therefore, we set a minimum limit for the absolute value of the shape function (Fig. 14(b)). This limit can be varied in accordance to the ability of the physical instrumentation used to produce the moiré grating lines. Optical representation of the one-dimensional moiré grating is shown in Fig. 14(c). Note that the width of the figure in Fig. 14(c) is artificially expanded for clarity (the actual width of this 1D moiré grating is 1 pixel).

4.6. Dynamic visual cryptography based on chaotically oscillating deformable moiré gratings

Let us consider a secret digital dichotomous image is presented in Fig. 15(a). Fig. 15(b) shows the secret image embedded into the

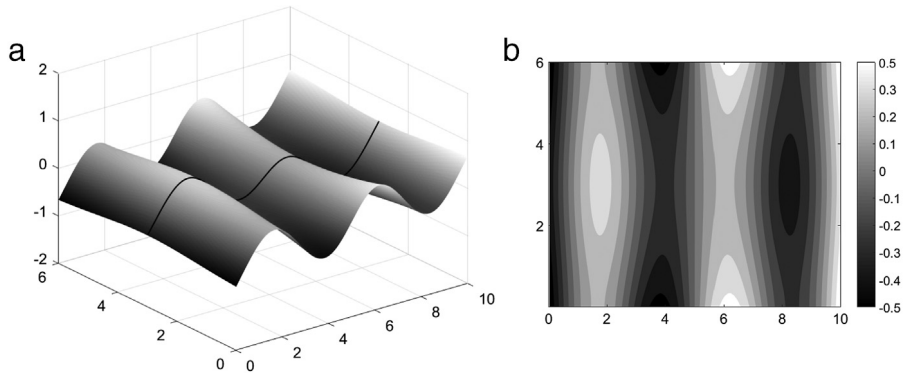

Fig. 13. The 17th Eigenshape of a free deformable plate: (a) 3D image; (b) the contour map.

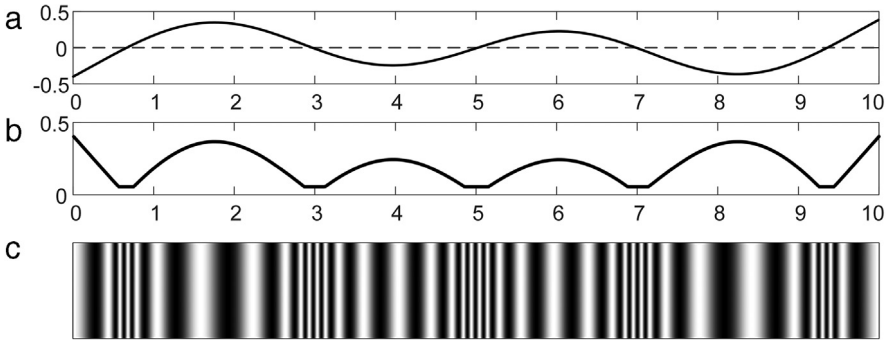

Fig. 14. A schematic diagram illustrating the construction of 1D moiré grating with the variable pitch: (a) the centerline of the 2D shape function representing the 17th Eigenshape; (b) absolute values of the shape function at the centerline; (c) optical representation of the 1D moiré grating.

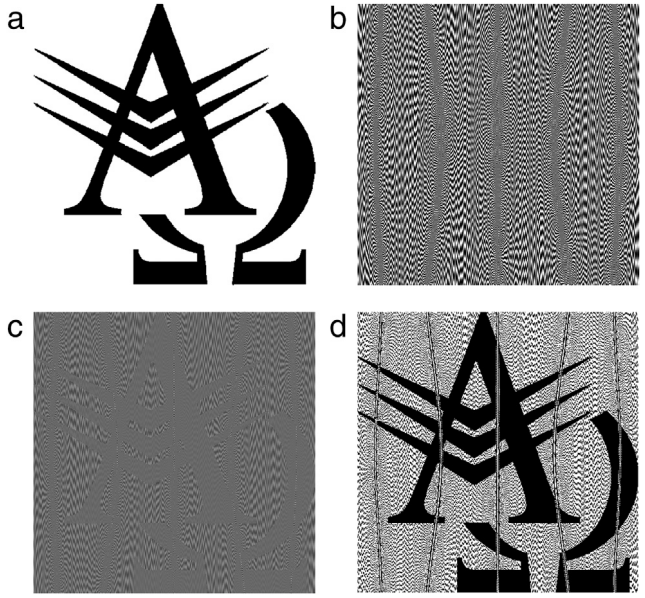

Fig. 15. Encoding and visual decoding of the secret image based on deformable grating and chaotic oscillation: (a) the secret image; (b) secret image encoded according to the 17th Eigenshape, the range of the variable pitch $\lambda(x)$ is $[0.015; 0.350]$; (c) visually decoded secret image in time-averaged image: the amplitude field of chaotic oscillations varies according the 17th Eigenshape, the range of in-plane deflections is $[-0.498; 0.740]$; (d) the contrast enhanced time-averaged cover image.

stationary moiré grating. Note that the variable pitch $\lambda(x)$ is preselected in such a way that it is proportional to the absolute value of the 17th Eigenshape (Fig. 13(a)) (varying in the interval between 0.015 and 0.350). Phase scrambling algorithm [11] is used to embed the secret image into the stochastic moiré grating — a naked eye cannot interpret the secret from the static cover image (Fig. 15(b)).

Fig. 15(c) shows the time-averaged image of Fig. 15(b) when the surface of the plate is oscillated according to the time function $x_1(t)$ (chaotic oscillation of the Rossler system). The shape function varies according to the 17th modal shape of the plate, the range of deflections is from −0.498 to 0.740. In other words, all vibration energy of chaotic oscillations is concentrated in the 17th Eigenmode of the plate. Contrast enhancement of Fig. 15(c) reveals the clear view of the decoded secret in the time-averaged mode.

Clearly, the modal shape of the plate serves as a key of visual decryption of the secret image. Optical time-averaging does not reveal the secret if the shape function of chaotic oscillations represents another modal shape of the plate. This fact is illustrated in Fig. 16 with shape functions of chaotic oscillations varying according to the 7st, 15th, 18th and 20th Eigenshapes.

5. Concluding remarks

An optical technique for image hiding in stochastic deformable and chaotically vibrating moiré gratings is presented in this paper. Special algorithms are used to embed the secret image into the cover moiré image. A computational device is not required to decrypt the secret image — the secret is leaked in the form of a pattern of time-averaged moiré fringes when the deformable moiré cover grating starts oscillating according to the chaotic law. Moreover, the parameters of chaotic vibrations must coincide with the ones used in the encryption phase of the secret image.

From the optical point of view, the proposed image hiding technique is based on the principles of time-averaged geometric moiré. It is well known that two basic goals exist within the research area of optical moiré based techniques. The first one is focused on the determination of physical properties of analyzed structures from the generated patterns

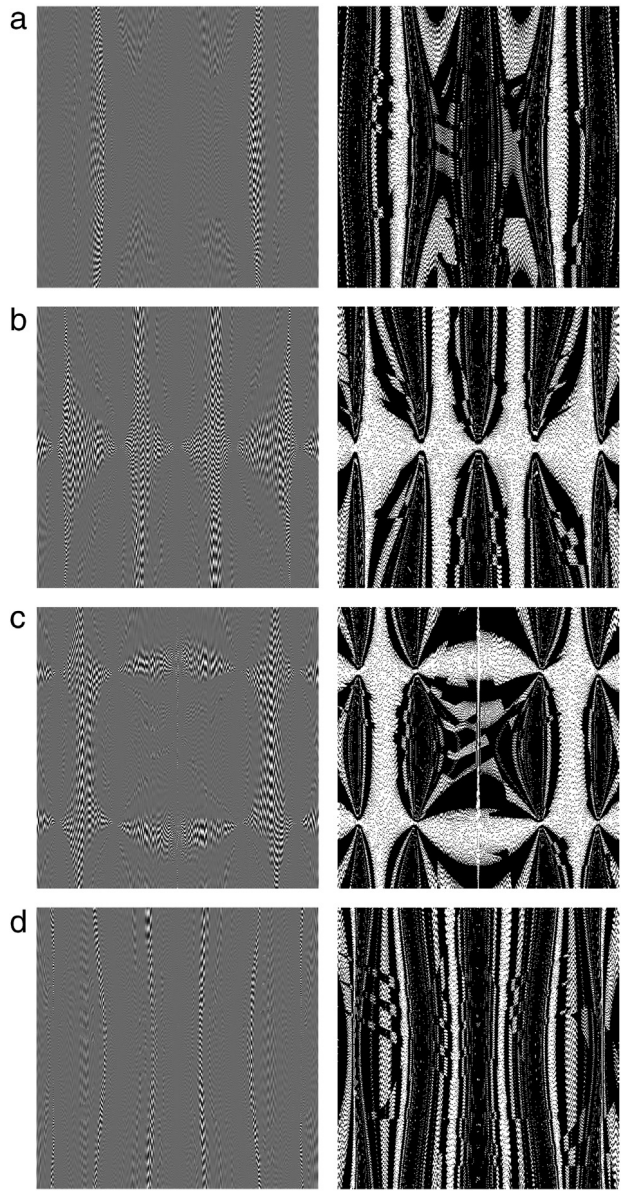

Fig. 16. Time-averaged (the left column) and contrast enhanced time-averaged (the right column) images. Chaotic oscillations according to an improper Eigenshape do not leak the secret in the time-averaged image: (a) oscillations according to the 7th Eigenshape, (b) the 15th Eigenshape; (c) the 18th Eigenshape; (d) the 20th Eigenshape.

of moiré fringes. The second one is based on the synthesis of a predefined pattern of fringes. Clearly, the proposed image hiding technique fits into the second group of optical moiré based image hiding methods.

The main difference of the proposed image hiding scheme to other mainstream image hiding methods (cryptography, steganography, watermarking) is based on the two main features – we do use a single cover image, and the secret is leaked when this cover image is oscillated according to the chaotic time function – and time-averaging optical techniques are used to reveal the secret.

Cryptography in general is used to change the data so that it is not readable (adversary can see there is a data communicated — but cannot understand it). Steganography hides and protects the communicating parties (adversary does not know of a secret communication). Watermarking is used to identify the ownership of the transmitted data. However, the proposed image hiding method belongs to a completely different class of visual information hiding techniques.

The presented optical decryption technique could find a comprehensive potential of applications. One of the potential application areas could be the development of an optical MEMS (micro-electro-mechanical) biochemical sensor. It is well known that changes in the vibration pattern of a biochemical sensor due to the accumulation of target substances on the active surfaces of the movable parts of the sensor (for example a micro-membrane) could be used as an effective indicator for monitoring the exposure to these substances [24,25]. Changes in the amplitude and the modal shape of harmonic vibrations have been successfully used to track the changes in the exposure to target substances [24,25]. However, it is well known that systems exhibiting chaotic vibrations are much more sensitive to perturbations if compared to systems performing stable limit-cycle harmonic vibrations. On the other hand, MEMS with chaotically oscillating movable parts are successfully developed. Merging the MEMS technology with the optical technology of image hiding in time-averaged cover images could be a promising area of applications and is a definite topic of future research.

Acknowledgments

Financial supports from the National Natural Science Foundation of China under Project No. 51475211 and the Lithuanian Science Council under Project No. MIP078/15 are acknowledged.

References

[1] A. Uchida, Applications of Nonlinear Dynamics and Synchronization, Wiley-VCH, Verlag, 2012.
[2] I.V. Izmailov, B.N. Poizner, D.A. Shergin, Spatial deterministic chaos in optical systems and methods of its modeling, Russian Phys. J. 47 (12) (2004) 1289–1296.
[3] E. Mercier, D. Wolfersberger, M. Sciamanna, High-frequency chaotic dynamics enabled by optical phase-conjugation, Sci. Rep. 6 (2016) 18988.
[4] Jian Liu, Hongzhen Jin, Lihong Ma, Yong Li, Weimin Jin, Optical color image encryption based on computer generated hologram and chaotic theory, Opt. Commun. 307 (2013) 76–79.
[5] A. Alfalou, C. Brosseau, Optical image compression and encryption methods, Adv. Opt. Photonics 1 (3) (2009) 589–636.
[6] Xiuli Chai, Yiran Chen, Lucie Broyde, A novel chaos-based image encryption algorithm using DNA sequence operations, Opt. Lasers Eng. 88 (2017) 197–213.
[7] Xingbin Liu, Wenbo Mei, Huiqian Du, Simultaneous image compression, fusion and encryption algorithm based on compressive sensing and chaos, Opt. Commun. 366 (2016) 22–32.
[8] Jun Lang, Color image encryption based on color blend and chaos permutation in the reality-preserving multiple-parameter fractional Fourier transform domain, Opt. Commun. 338 (2015) 181–192.
[9] Liansheng Sui, Minjie Xu, Ailing Tian, Optical noise-free image encryption based on quick response code and high dimension chaotic system in gyrator transform domain, Opt. Lasers Eng. 91 (2017) 106–114.
[10] D. Sweet, E. Ott, J.A. Yorke, Topology in chaotic scattering, Nature 399 (1999) 315.
[11] M. Ragulskis, A. Aleksa, Image hiding based on time-averaging moiré, Opt. Commun. 282 (2009) 2752–2759.
[12] P. Palevicius, M. Ragulskis, Image communication scheme based on dynamic visual cryptography and computer generated holography, Opt. Commun. 335 (2015) 161–167.
[13] V. Petrauskiene, R. Palivonaite, A. Aleksa, M. Ragulskis, Dynamic visual cryptography based on chaotic oscillations, Commun. Nonlinear Sci. Numer. Simul. 19 (2013) 112–120.
[14] V. Petrauskiene, A. Survila, A. Fedaravicius, M. Ragulskis, Dynamic visual cryptography for optical assessment of chaotic oscillations, Opt. Laser Technol. 57 (2014) 129–135.
[15] A.S. Kobayashi, Handbook on Experimental Mechanics, second ed., SEM, Bethel, CT, 2000.
[16] K. Patorski, M. Kujawinska, Handbook on the Moiré Fringe Technique, Elsevier, Amsterdam, 1993.
[17] C.Y. Liang, Y.Y. Hung, A.J. Durelli, J.D. Hovanesian, Time-averaged moiré method for in-plane vibration analysis, J. Sound Vib. 62 (1979) 267–275.
[18] M. Ragulskis, L. Saunoriene, R. Maskeliunas, The structure of moiré grating lines and its influence to time-averaged fringes, Exp. Tech. (2009) 60–64 March/April.
[19] M. Ragulskis, Z. Navickas, Time-average moiré–back to the basics, Exp. Mech. 49 (8) (2009) 439–450.
[20] M. Ragulskis, M. Sanjuan, L. Saunoriene, Applicability of time-average moiré techniques for chaotic oscillations, Phys. Rev. E 76 (2007) 036208.

[21] R. Hilborn, Chaos and Nonlinear Dynamics: An Introduction for Scientists and Engineers, Oxford University Press, Oxford, 1994.
[22] The Concise Encyclopedia of Statistics, Springer, Verlag, 2008.
[23] P.G. Biltta, M.P. Deepika, Cheating prevention schemes for visual cryptography, Int. J. Eng. Res. Technol. 4 (7) (2015) 324–328.
[24] I. Dufour, S.M. Heinrich, Fabien Joe, Theoretical analysis of strong-axis bending mode vibrations for resonant microcantilever (bio)chemical sensors in gas or liquid phase, J. Micro-Electro-Mech. Syst. 16 (2007) 44–49.
[25] Huayong Wu, Shenjie Zhou, Free vibrations of sensor diaphragm with residual stress coupled with liquids, J. Appl. Phys. 115 (8) (2014) 084303.